Journal of Alloys and Compounds 977 (2024) 173400

Contents lists available at ScienceDirect

Journal of Alloys and Compounds

journal homepage: www.elsevier.com/locate/jalcom

A new approach to the synthesis of $CuMoO_4$ nanoparticles with mechanistic insight into the sunlight-assisted degradation of textile pollutants and antibacterial activity evaluation

Rusul Alabada [a], Asif Ayub [b,*], Yathrib Ajaj [c], Subrahmanya Ishwar Bhat [d], Riyadh H. Alshammari [e], Aigul Abduldayeva [f], Ali Imran Mallhi [g], Zubair Ahmad [h], Rasha M.K. Mohamed [i]

[a] Al-Muthanna University, College of Nursing, Muthanna State, Samawah 66001, Iraq
[b] Institute of Chemistry, The Islamia University of Bahawalpur, Bahawalpur 63100, Pakistan
[c] Engineering Department, Faculty of Engineering and Computer Science, German University of Technology, Halban, Oman
[d] Department of Chemistry, NMAM Institute of Technology, Nitte, Karnataka 574110, India
[e] Department of Chemistry, College of Science, King Saud University, Riyadh 11451, Saudi Arabia
[f] Department of Research Institute of Preventive Medicine named Academician E.Dalenov, Astana Medical University, Astana 010000, Kazakhstan
[g] Department of Applied Chemistry, Government College University Faisalabad, Punjab 38000, Pakistan
[h] School of Chemical Engineering, Yeungnam University, 280 Daehak-ro, Gyeongsan, Gyeongbuk 38541, Republic of Korea
[i] Department of Chemistry, Faculty of Science, Assiut University, P.O. Box, 71515, Assiut, Egypt

ARTICLE INFO

Keywords:
AOP
Band gap
$CuMoO_4$
Degradation
Thermal decomposition

ABSTRACT

$CuMoO_4$ nanoparticles (NPs) were synthesized by a thermal decomposition followed by a precipitation method. Analytical techniques such as FE-SEM, EDS, HR-TEM, XRD, FTIR, UV–visible, PL, and XPS were used to characterize the structural, optical, and photocatalytic properties of $CuMoO_4$. As per XRD analysis, the structure of $CuMoO_4$ NPs with different Cu concentrations was consistent, however, their crystallinities were changed. The band gap of $CuMoO_4$ with various concentrations of Cu (0.1, 0.2, and 0.3 M) was estimated to be 1.97 eV, 1.86 eV, and 1.44 eV, respectively. The electrical conductivity of 0.3 M $CuMoO_4$ NPs was greater than other synthesized nanocomposites. Methylene Blue (MB) mineralization in an aqueous medium after 180 min of exposure to sunlight was investigated to study the photocatalytic activities of all $CuMoO_4$ composites. As per the PL study, the 0.3 M $CuMoO_4$ NPs exhibited better photocatalytic efficiency due to their low electron-hole recombination rate. Experimental parameters like the MB concentration, catalyst dosage, and the solution pH were evaluated to optimize the experimental conditions. The *in-situ* capture analysis proposed a plausible mechanism for the photocatalytic degradation of MB. The two main active species identified for MB degradation were superoxide radical anions and hydroxyl radicals. The repeated photocatalytic MB degradation verified the high level of reusability of 0.3 M $CuMoO_4$. The well-diffusion technique was utilized to examine the antibacterial activity of 0.3 M $CuMoO_4$ NPs against gram-positive (*Salmonella typhi*) and gram-negative (*Streptococcus mutans*) bacterial strains. The optimized $CuMoO_4$ showed excellent promise for application in the field of photocatalysis, electrocatalytic and antibacterial activity.

1. Introduction

Pure water is regarded as the most vital need of daily living; at present, the quanity and quality of drinking water are inadequate to satisfy the necessities of human existence [1]. Nearly 748 million people were unaware that there is not enough clean water to drink. By 2050, the quantity of water required by industries like manufacturing will have increased by 400% [2]. The volume of wastewater released increases along with the increase in industrialization including textiles, paper mills, concrete, plastic, rubber, and pharmaceuticals. Methylene blue (MB) is a colorant dye and used to stain wool, silk, cotton, and is also used in biological staining. MB is dangerous to aquatic habitats owing to

* Corresponding author.
E-mail address: asif.chemist45@gmail.com (A. Ayub).

https://doi.org/10.1016/j.jallcom.2023.173400
Received 11 August 2023; Received in revised form 11 November 2023; Accepted 29 December 2023
Available online 2 January 2024

its interference with photosynthesis, and its toxicity offers difficulties to ecosystems and causes some major environmental issues that impact aquatic life as well as human health [3]. A large portion of the textile dyes (60–70%) are azo compounds, which account for 20% of the total organic pollutants in water delivered by textile industries [4]. Aromatic dyes are very hazardous and challenging to degrade due to their comparatively stable chemical structures. [5,6]. Hence, among various types of pollution, it is important to develop dependable, reliable, and financially viable approaches for wastewater treatment.

Several practical approaches have been developed to effectively remove organic contaminants from wastewater. The conventional wastewater treatment used to degrade these pollutants resulted in the transfer of pollutants from one form to another that is more hazardous than the original pollutant molecules [7]. Considering the aforementioned issues, it is necessary to establish a process that can considerably destroy the contaminants found in effluent. In this context, the utilization of advanced oxidation processes (AOPs) based on semiconductors has gained attention due to their ability to mineralize organic contaminants in aqueous solutions [8]. Various semiconductor materials including TiO_2, ZnO, MoO_3, SnO_2, and WO_3, have been utilized for mineralization of harmful organic contaminants under UV or visible light all over the years [9]. Among all natural resources for energy, solar energy is regarded as the most effective, conveniently easily accessible, sustainable, and global energy source. Visible light provides 43% of the energy in the solar spectrum, whereas UV light contributes just 4%. So it is important to fabricate such photocatalysts that use visible light to mineralize pollutants [10].

Compounds containing metal molybdate, denoted by the formulation $MMoO_4$, are a significant class of inorganic materials, with diverse appliances such as magnetic materials, photoluminescence, high electrical conductivity, symmetric capacitors, thermal stability, and elasticity, optical transparency, pigments, supercapacitors, lithium-ion batteries, photocatalysts, and radio generators [11]. Additionally, metal molybdate, a transition metal, is extensively used as a photocatalyst to degrade industrial organic pollutants, like organic colored compounds and their intermediates, that are harmful to the environment and contaminate the ecosystem because they contain excessive oxygen vacancies, which are essential to remove in photocatalysis [12]. In particular, due to its numerous uses, the copper molybdate nanocatalyst, $CuMoO_4$ was extensively used [13].

In this work, a simple thermal decomposition method followed by a precipitation method has been used to synthesize $CuMoO_4$ with varied Cu mass molarities. MB mineralization under sunlight irradiation has been used to study $CuMoO_4$ photocatalytic properties. The novelty of the present work is, that there are no other studies in the literature about $CuMoO_4$ NPs synthesized by the thermal decomposition followed by precipitation method. Based on the characterization and analytical results, a mechanism for the photocatalyst's increased photocatalytic performance has also been proposed, in addition, the electrocatalytic and antibacterial activities were also studied. By studying the degradation of dye, the potential usability of $CuMoO_4$ NPs was evaluated. Additionally, the species involved in the mineralization process were analysed by scavenger study which was used to explain and clarify the photocatalytic degradation mechanism of MB dye.

2. Experimental section

2.1. Materials and methods

The copper nitrate trihydrate $Cu(NO_3)_2.3\ H_2O$, ammonium hepta-molybdate tetrahydrate $(NH_4)_6Mo_7O_{24}.4\ H_2O$, and ammonia solution 25% were purchased from Sigma Aldrich. Analytical-grade chemicals were employed without any further purification.

2.2. Synthesis of $CuMoO_4$ NPs

The commercially available ammonium hepta-molybdate tetrahydrate $(NH_4)_6Mo_7O_{24}.4\ H_2O$ (5 g) was thermally converted into MoO_3 over 3.5 h at 400 °C. To achive a uniform MoO_3 dispersion, a suitable quantity (0.5 g) of freshly obtained MoO_3 was added to the 25 mL of double-distilled water and stirred for around 30 min. 2.5 mL of $NH_3{\cdot}H_2O$ solution was poured in the MoO_3 suspension to get the $(NH_4)_2MoO_4$ clear solution. After that, the solution was stirred for 30 min. Further, different concentrations of 25 mL $CuNO_3.3\ H_2O$ [0.1 M (0.604 g), 0.2 M (1.208 g), and 0.3 M (1.812 g)] were slowly added to the aforementioned solution mixture. Upon copper solution addition, the solution pH reached 7 and this change in pH leads to the precipitation of $Cu_3(MoO_4)_2(OH)_2$ due to the interaction of Cu and Mo ions in solution [14]. The freshly prepared precipitates of $CuMoO_4$ were rinsed with DI water, and then alcohol. The prepared precipitates were dried at 80 °C in the oven for 6 h and finally calcined for 2 h at 500 ℃. $CuMoO_4$ prepared by different concentrations of copper were labelled as 0.1 M $CuMoO_4$, 0.2 M $CuMoO_4$, and 0.3 M $CuMoO_4$. The stepwise synthesis procedure is depicted in Scheme 1.

2.3. Photocatalytic activity

Photocatalytic MB degradation in aqueous solution under sunlight was investigated to measure the photocatalytic efficiency of $CuMoO_4$. Degradation experiments were performed from 11 a.m. to 3 p.m. at Al-Muthanna University, Iraq in April 2023. All of the synthesized catalysts i.e., 0.1 M $CuMoO_4$, 0.2 M $CuMoO_4$, and 0.3 M $CuMoO_4$ were employed to carry out the photocatalytic degradation activity. In a typical test, 5 mg of catalyst was added to 10 ppm of MB solution in 100 mL solution. Before being exposed to sunlight, the suspension was agitated periodically in the dark for 30 min to establish an equilibrium between the adsorption-desorption of the catalysts and the contaminants. 5.0 mL of suspension was taken out during solar irradiation at 30 min regular intervals and filtered to get rid of the catalysts from the MB solution. The UV–visible 4000 spectrophotometer was utilized to measure the concentration of MB at its distinctive absorption peak (664 nm). The degradation efficiency (η) of MB dye was evaluated using Eq. (1).

$$\eta = \frac{C_0 - C}{C_o} * 100 \tag{1}$$

Where C_o represents the initial concentration of MB and C represents the MB concentration upon light exposure [15].

The active species produced in the photocatalytic degradation of MB dye with 0.3 M $CuMoO_4$ NPs were extensively explored *in situ* through capture studies. Scavengers like 1 mM silver nitrate ($AgNO_3$), disodium ethylene diamine tetraacetate (Na_2-EDTA), isopropanol (IPA), and p-benzoquinone (p-BQ) were utilized in the photocatalytic process to inhibit electrons (e^-), holes (h^+), hydroxyl radicals ($^{\bullet}OH$), and superoxide radicals ($O_2^{\bullet-}$).

Additionally, the reusability of 0.3 M $CuMoO_4$ was carried out for four cycles under the same conditions as in the photocatalytic experiment. The photocatalyst and the leftover contaminant were separated using centrifugation. To remove any unwanted components, the catalyst was cleaned with water and ethanol before each subsequent cycle. The material was then dried for 6 h at 120 °C, and reused for the subsequent cycles.

2.4. Zero-point charge

The zero-point charge (pH_{ZPC}) was calculated to gain information about the surface charge of $CuMoO_4$ NPs. Using the salt addition method, the pH_{ZPC} was calculated. In the standard procedure, 20 mg of $CuMoO_4$ NPs were added to round-bottomed flasks having 40 mL of $NaNO_3$ solution (0.1 M) at various pH levels (3 to 11). On an orbital

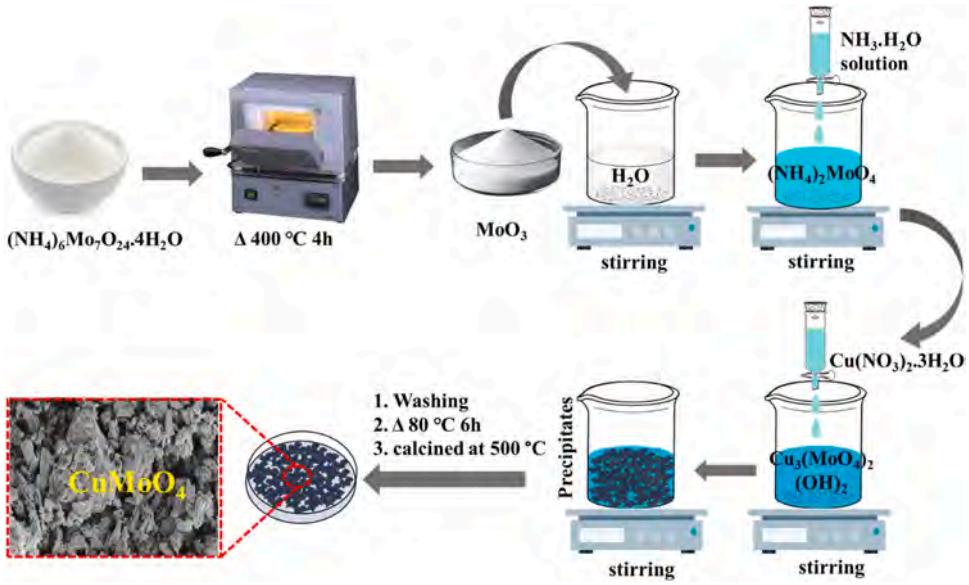

Scheme 1. Synthesis of $CuMoO_4$ NPs by thermal decomposition method.

shaker, the flasks were shaken for 24 h at a rate of 200 rpm. The pH value was then measured after the flasks had been well agitated. Finally, by plotting the ΔpH against the original pH, the pH_{ZPC} value was calculated.

2.5. Antibacterial activity

2.5.1. Extract preparation

After solubilization, the samples underwent a 10-min sonication. Then, a stock of 5 mg/mL was prepared and stored for further usage. In this study, the bacteria *Streptococcus mutans* and *Salmonella typhi* were used.

2.5.2. Preparation of inoculums

From the stock solution, the bacteria were transported to LB agar and cultured at 37 °C for a night. LB broth was used to grow one colony from the plate, which was then incubated at 37 °C for 24 h. The McFarland 0.5 turbid standard (1.5 108 CFU/mL) was used as the standard for the spectrophotometric adjustment of the turbidity of the bacterial solution.

2.5.3. Antibacterial activity by well diffusion method

Using the well-diffusion technique, it was determined that 0.3 M $CuMoO_4$ had any antibacterial effects on gram-positive (*Salmonella typhi*) and gram-negative (*Streptococcus mutans*) bacterial strains. To create test plates with a diameter of approximately 10 cm, 20 mL of LB agar was used. 100 μL of a 24-h bacterial culture (1.5108 CFU/mL) was placed once the medium had solidified, and it was distributed evenly across the plates using an L-shaped loop. Next, add 50 μL of each sample, at a concentration of 5 mg/mL, to a well with a diameter of about 6 mm. A 30 μg/40 μL commercial standard of streptomycin was employed, and blank wells were then filled with a sterile medium. After loading, plates were maintained sterile until all test chemicals had been absorbed. Plates were incubated in an appropriate gaseous phase for 24 h at 37 °C. Following the incubation period, measurements and records were made of the wells around zones of microbial growth inhibition. The shortest distance (in mm) between both the sample's outside boundary and the starting of microbial growth was used to define the inhibitory zone.

2.6. Materials characterization

The structure and crystalline nature of the $CuMoO_4$ powders were examined by an X-ray diffractometer (XRD) (BRUKER: D8 advance) by CuK_α radiation ($\lambda = 0.154$ nm), by measurements of 2θ values ranging from 20° to 80° at a speed of 5°/min. The Carl-Zeiss AG-ULTRA 55 microscope and a Talos F200S G2 were utilized as SEM and TEM for the morphological size distribution of the sample's characterization. The IR spectra of KBr pellets were recorded using a Perkin Elmer spectra RX-1 type spectrophotometer. The UV-Vis spectroscopy was carried out by a UV–visible spectrophotometer, model SB 4000, made by Ocean Optics, U.S.A. The photoluminescence investigation was performed using a spectrofluorimeter FP8200 from Jasco in Japan. The valence states of several elements have been investigated using an XPS analyzer by Mg-K_α radiation, model: Kratos, Axis DLD.

3. Results and discussion

3.1. Morphological analysis

By using Field Emission Scanning Electron Microscope (FE-SEM) analysis, the $CuMoO_4$ NP's structure and morphology were characterized (Fig. 1**a-c**). The FE-SEM images showed that all 0.1 and 0.2 M $CuMoO_4$ exhibit an agglomerated irregular morphology and 0.3 M $CuMoO_4$ also shows agglomerated irregular morphology with square-like shapes in a size range of 1 μm [16]. The elemental composition and purity of 0.3 M $CuMoO_4$ NPs have been investigated using EDX analysis. EDX examination (Fig. 1**d-f**) verified that Cu, O, and Mo were present in the 0.3 M $CuMoO_4$ NPs.

Figs. 1**g and** 1**h** display TEM images and selected-area electron diffraction (SAED) pattern of 0.3 M $CuMoO_4$ NPs. The $CuMoO_4$ powders' nanostructure and interface characteristics were further examined. The morphology of $CuMoO_4$ exhibits an agglomerated irregular sphere-like morphology as depicted in Fig. 1**g**, and the aforementioned findings are in agreement with those from the SEM analysis of $CuMoO_4$ NPs. The ring formation in the SAED pattern is shown in Fig. 1**i**, which can help to confirm that the material $CuMoO_4$ was polydisperse and crystalline in nature [14].

3.2. Structural analysis (XRD)

Phase purity and crystallinity of the produced samples were investigated using XRD. The XRD patterns of 0.1 M $CuMoO_4$, 0.2 M $CuMoO_4$, and 0.3 M $CuMoO_4$ are shown in Fig. 2**a**. $CuMoO_4$ XRD patterns show that all diffraction peaks match the standard value very well (PDF#73–0488), confirming that the materials were successfully

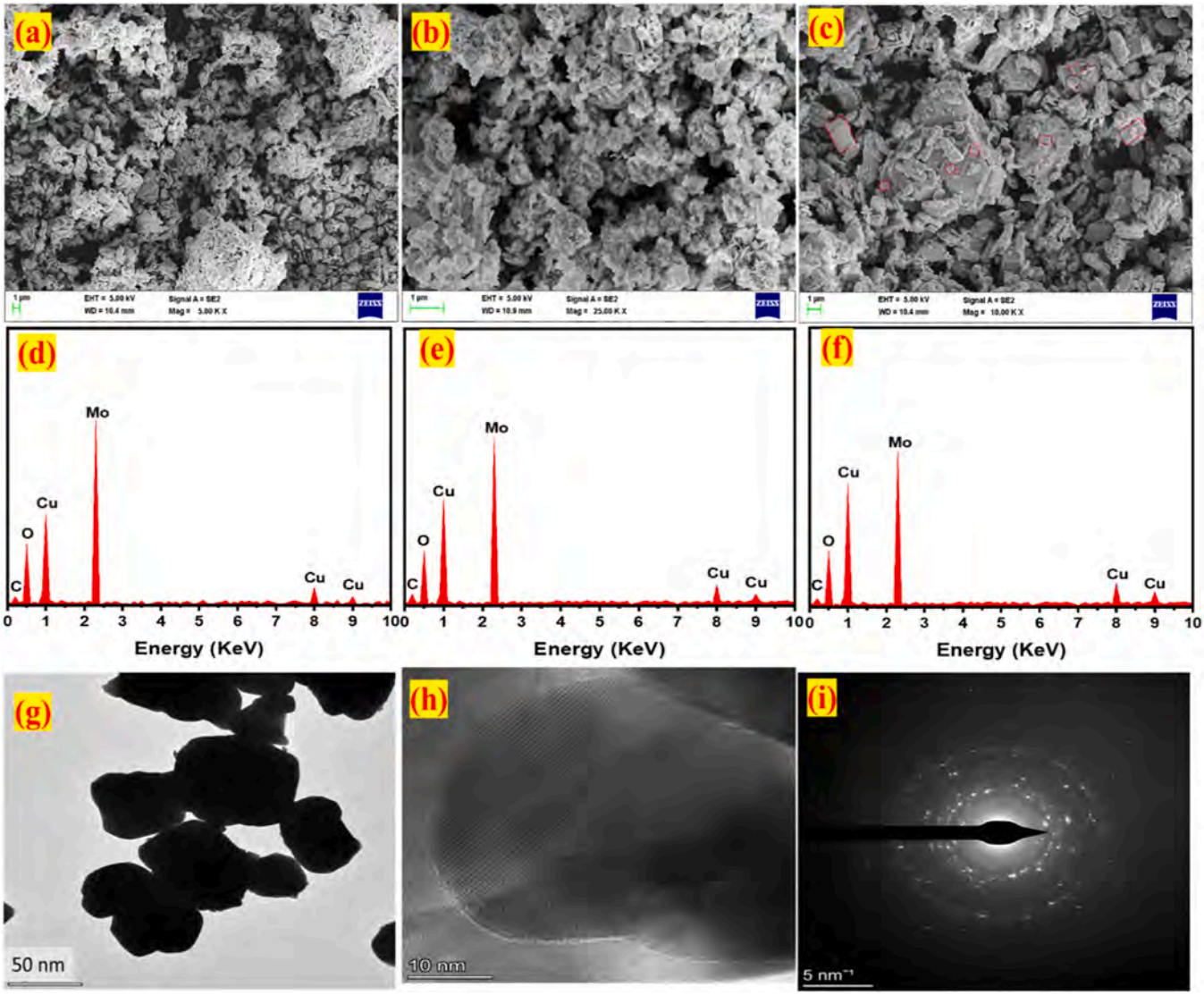

Fig. 1. FE-SEM images of (a) 0.1 M, (b) 0.2 M, and (c) 0.3 M $CuMoO_4$ NPs, EDX of (d) 0.1 M, (e) 0.2 M, and (f) 0.3 M $CuMoO_4$ NPs, (g and h) HR-TEM images, and (i) SAED pattern of 0.3 M $CuMoO_4$ NPs.

prepared [14]. The reflections of the $CuMoO_4$ planes (−101), (101), (201), (−202), and (021), respectively, are represented by the characteristic 2θ positions of 11.98, 15.68, 23.79, 26.42, and 32.85. Fig. 2**a** also demonstrates that as the copper concentration increases from 0.1 M to 0.3 M in $CuMoO_4$, also rises the intensity of the peaks. Cu was effectively incorporated into MoO_4 to form $CuMoO_4$, as evidenced by the increase in peak intensity. There are no more impurity peaks to be seen. The Full-Width Half Maxima (FWHM) of the XRD peaks was used for determining the average crystalline size, which was determined to be 41.28 nm, 44.25 nm, and 49.78 nm, respectively [14,17]. When the concentration of copper in a crystalline material increases, it also increases the crystalline size. This happens due to the incorporation of copper atoms which damage the normal lattice structure. As the concentration of copper increases, it causes the lattice strain and defect, leading the crystal to grow in size accommodate more atoms, and attain stability. This results in bigger crystalline domains and an increase in overall crystalline size [18].

The Scherrer formula stated in Eq. (2) was employed to find out the crystalline size of the synthesized samples.

$$(D) = \frac{0.9\lambda}{\beta\cos\theta} \tag{2}$$

Where D is the NP's crystalline size, λ is the radiation's wavelength, β is FWHM in radians, and θ is the Bragg's diffraction angle.

3.3. FTIR

FT-IR spectra were used to examine the functional groups and bonding vibrations in $CuMoO_4$ NPs. Fig. 2**b** demonstrates that the synthesized $CuMoO_4$ absorption bands were mainly localized within a 1000 cm^{-1} range. The absorption peaks at 965, 940, 901, 821, 718, and 524 cm^{-1} are comparable with previously reported data [19]. The absorption peaks can be seen in the $CuMoO_4$ spectrum at 3156 cm^{-1}, which represents the O-H stretching vibration and Mo = O peak at 965 cm^{-1}, Mo-O-Mo stretching vibration peak at 821 cm^{-1}, and Cu-O bond absorption peak at 524 cm^{-1} [16].

3.4. Optical analysis

3.4.1. UV-vis spectral analysis

The Impact of Cu content on $CuMoO_4$'s optical properties was studied *via* UV-Vis DRS analysis. The absorption spectra of varied Cu concentrations in $CuMoO_4$ NPs are shown in Fig. 2**c**. The results show that the transition of electrons from VB to CB is the major cause of the absorption

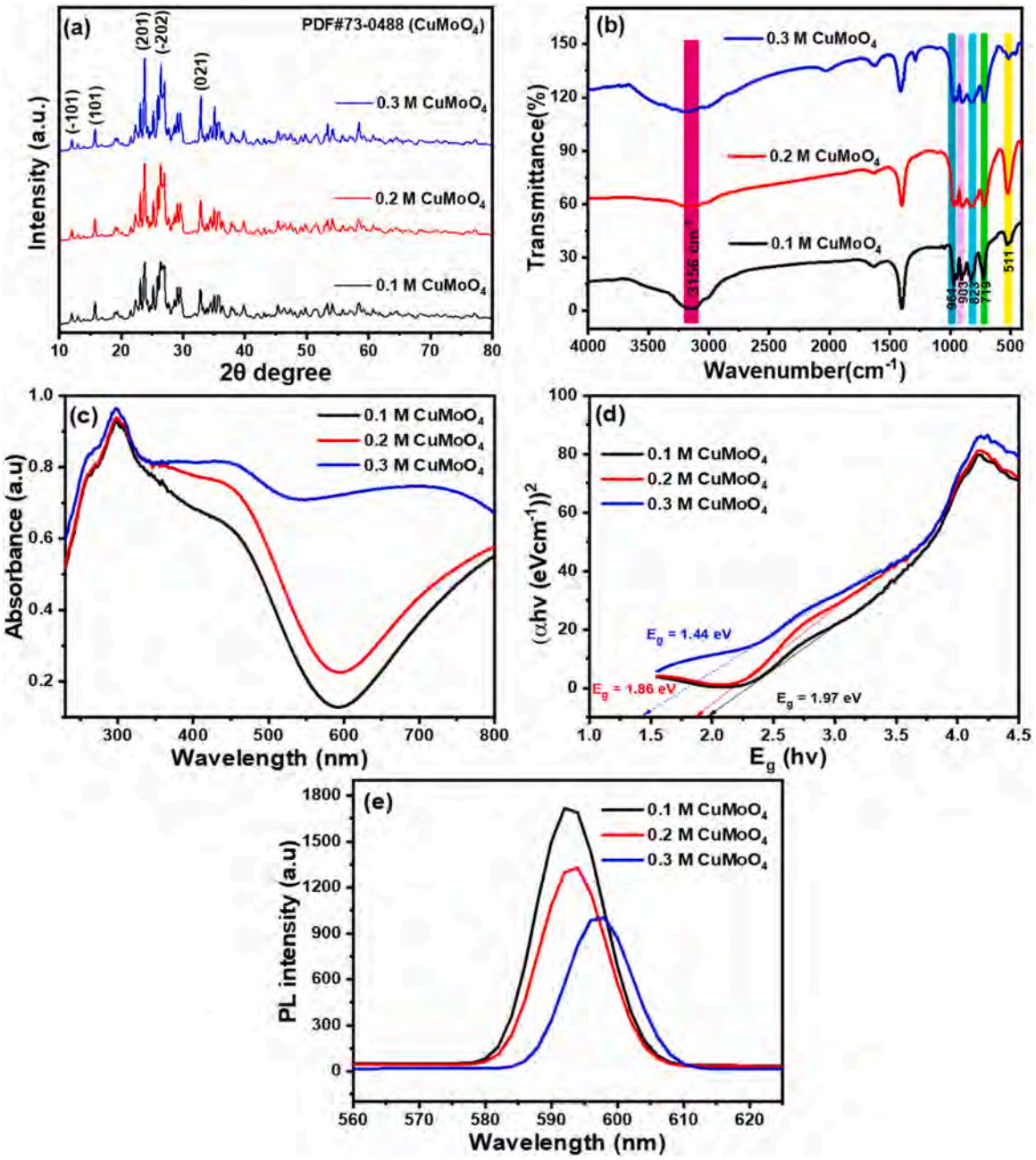

Fig. 2. (a) XRD pattern, (b) FTIR spectra, (c) UV–visible absorbance spectra, (d) Tauc plot (band gap), and (e) Photoluminescence spectra of 0.1 M, 0.2 M, and 0.3 M $CuMoO_4$ NPs.

at 445 nm in $CuMoO_4$ NPs. The charge-transfer transitions between the Cu ion's *d* electrons in the $CuMoO_4$ conduction or valence band may be responsible for a shift in the absorption edge. $CuMoO_4$ NPs show an absorbance shift towards higher wavelengths when the concentration of Cu in the material increases. This indicates the introduction of Cu into MoO_4, which may cause an impurity state or defects between the VB and CB of the material. Cu may introduce substitutional and interstitial defects in the crystal lattice of $CuMoO_4$ to alter its electronic properties.

A drop in absorption band at 600 nm in UV–visible spectra of nanocomposite has also been observed, this might be related to a phenomenon known as "plasmon resonance." At this wavelength, nanoparticles may display an oscillation of conduction electrons, reducing their capacity to absorb light and providing a decrease in the absorption spectrum [20].

The synthesized samples exhibit an absorbance shift towards higher wavelengths in the following order: 0.1 M > 0.2 M > 0.3 M. The charge-transfer transitions between the Cu ion's *d* electrons in the $CuMoO_4$ conduction or valence band may be responsible for a shift in the absorption edge. The produced samples' optical bandgap energies were calculated using the Tauc equation, Eq.3, and the plots are displayed in Fig. 2**d** [21].

$$(\alpha hv)^{1/n} = A\,(hv - Eg) \tag{3}$$

Fig. 2**d** illustrates a graph between $(\alpha hv)^2$ and E_g that can be utilized to compute the band gap of synthesized NPs. The band gaps of 0.1 M $CuMoO_4$, 0.2 M $CuMoO_4$, and 0.3 M $CuMoO_4$ NPs were estimated to be 1.97 eV, 1.86 eV, and 1.44 eV, respectively. The reduction in the optical band gap seen with increasing Cu incorporation might be attributed to structural deformation in the MoO_4 NPs caused by replacing with either substitutional or interstitial molybdenum ions in the MoO_4 lattice by Cu

ions [22]. The results show that the absorption of $CuMoO_4$ is in the visible area, hence all irradiation studies were performed with a sunlight source [23,24].

3.4.2. Photoluminescence (PL) spectra analysis

The Photoluminescence (PL) spectra analysis was used to study the optical characteristics of $CuMoO_4$ NPs. On the other hand, PL spectroscopy is a technique for investigating both the charge carrier transfer process on the surface of photocatalysts and the recombination rate associated with the photoexcited electrons and holes [14]. In the $[MoO_4]$ ion complex, the O 2p and Mo 4d orbitals in the $CuMoO_4$ emission spectrum typically show charge-transfer transitions. Fig. 2**e** depicts the PL spectra of 0.1 M $CuMoO_4$, 0.2 M $CuMoO_4$, and 0.3 M $CuMoO_4$ NPs with an excitation wavelength of 578 nm and a sharp peak was observed at 592 nm [25]. The PL spectra intensity for 0.3 M $CuMoO_4$ was much lower than for 0.1 $CuMoO_4$, and 0.2 M $CuMoO_4$. Recombination of electron-hole pairs in $CuMoO_4$ is inhibited by increasing Cu concentration. This is because Cu provides more charge carriers, either holes or electrons, which lowers the chance of carriers recombining and increases carrier density, thereby decreasing electron-hole pair recombination [26]. This showed that the progress of photocatalytic processes was enhanced by 0.3 M $CuMoO_4$ because it had a lower recombining rate of photoexcited electron-hole pairs [27].

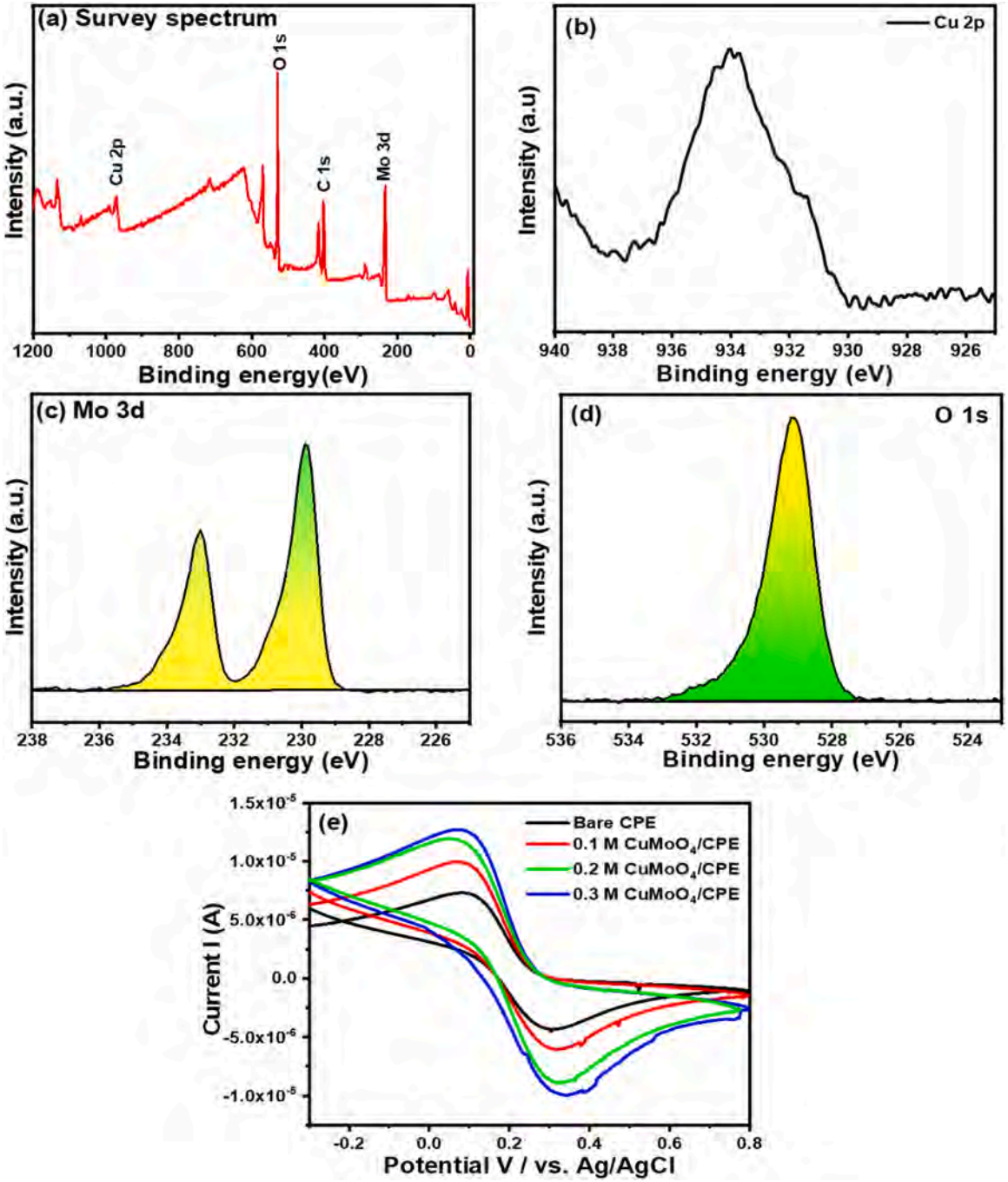

Fig. 3. XPS spectra showing (a) survey spectrum, (b) Cu-2p, (c) Mo-3d, (d) O-1 s of 0.3 M $CuMoO_4$ NPs and (e) Overlay of the cyclic voltammetric response of bare CPE, modified 0.1 M $CuMoO_4$/CPE, 0.2 M $CuMoO_4$/CPE, and 0.3 M $CuMoO_4$/CPE NPs in the presence of 0.1 M KCl containing 5 mM $[Fe(CN)_6]^{3-/4-}$ ions.

3.5. XPS analysis

We employed the XPS technique to investigate the chemical composition and bonding configuration in $CuMoO_4$ to understand more about the interfacial electronic structures. Fig. 3**a** displays the survey XPS spectra of $CuMoO_4$. The C, Cu, Mo, and O elements are also seen in the survey XPS spectra of $CuMoO_4$. The peak at 284.0 eV in the survey XPS spectra was attributed to the adventitious carbon in $CuMoO_4$, and the adventitious carbon was found to be standard carbon (Fig. 3**a**). A significant peak at 934.0 eV in the fitted Cu *2p* in $CuMoO_4$ peaks was attributed to the $2p_{3/2}$ core level of Cu^{2+} (Fig. 3**b**). In $CuMoO_4$, Mo *3d* has a binding energy of 229.8 or 232.7 eV (Fig. 3**c**) The asymmetric peak at 528.8 eV in the O *1 s* spectra of $CuMoO_4$ was attributed to the binding energy of O_2 species representative of oxide materials. $CuMoO_4$'s surface-adsorbed oxygen species may be responsible for the shoulder peak that was seen at 529.8 eV (Fig. 3**d**) [14].

3.6. Charge transfer behaviour of modified electrodes

Cyclic Voltammetry curves of 0.1 M $CuMoO_4$, 0.2 M $CuMoO_4$, and 0.3 M $CuMoO_4$ were analyzed in 0.2 M phosphate buffer (pH-7) with 5 mM $K_3[Fe(CN)_6]$ and $K_4[Fe(CN)_6]$ as an electrolyte to confirm the improved conductivity of $CuMoO_4$ NPs. Fig. 3**e** represents the charge transfer behavior of electrodes made of bare Carbon Paste Electrode (CPE), 0.1 M $CuMoO_4$/CPE, 0.2 M $CuMoO_4$/CPE, and 0.3 M $CuMoO_4$/CPE. When 0.1 M $CuMoO_4$/CPE was increased to 0.3 M $CuMoO_4$/CPE, the redox peak currents enhanced significantly and the redox peak potential moved more positively, signifying that 0.3 M $CuMoO_4$/CPE has electrocatalytic activity. These high peak current intensities were observed for the $[Fe(CN)_6]^{3-}/[Fe(CN)_6]^{4-}$ system at a scan rate of 50 mV s^{-1}. Additionally, it was found that 0.3 M $CuMoO_4$/CPE has an electrical conductivity that is greater magnitude than CPE, 0.1 M $CuMoO_4$/CPE, and 0.2 M $CuMoO_4$/CPE. This is due to the modified CPE's ability to function as a conductor and enable quick charge transfer in solution. [28].

3.7. Evaluation of the photocatalytic activity with different concentrations of $CuMoO_4$ NPs

To test the influence of Cu concentration (0.1, 0.2, and 0.3 M) in $CuMoO_4$ NPs, the degradation of MB was studied. The results revealed that increasing the Cu content in the crystalline lattice of $CuMoO_4$ NPs from 0.1 M to 0.3 M enhanced the photocatalytic degradation efficiency in 180 min of reaction time. Fig. 4**a** shows the MB dye degrading efficiency of various catalysts at 30-minute time intervals of up to 180 min. Fig. 4**a** shows that the mineralization of the MB dye is 80.61%, 85.03%, and 92.43% for 0.1 M $CuMoO_4$, 0.2 M $CuMoO_4$, and 0.3 M $CuMoO_4$ NPs, respectively [29]. The concentration of MB dye decreased as the irradiation period increased (Fig. 4**b**). Fig. 4**c** depicts the absorption spectrum results for the best 0.3 M $CuMoO_4$ NPs sample for MB degradation. According to the results presented in Fig. 4**a-c**, raising Cu concentrations in the crystalline structure of the $CuMoO_4$ NPs improved their photocatalytic activity. The PL results revealed that 0.3 M $CuMoO_4$ NP has lowered PL intensity compared to 0.1 $CuMoO_4$, and 0.2 M $CuMoO_4$ (Fig. 2**e**). The PL spectra may be used to explain that the 0.3 M $CuMoO_4$ NPs have higher photocatalytic activity. The observation indicates that introducing more Cu ions to the crystalline lattice of $CuMoO_4$ NPs decreases the electron-hole pairs recombination rate, hence increasing the MB mineralization.

3.7.1. Effect of dose

One of the key factors influencing the degrading performance is the catalyst dose. The photocatalytic degradation experiment was conducted using different catalyst doses of 0.3 M $CuMoO_4$ such as 5, 10, 15, and 20 mg, with 10 ppm MB dye concentration while maintaining the dye solution at natural pH. Fig. 5**a** shows that for 5, 10, 15, and 20 mg of 0.3 M $CuMoO_4$, the photocatalytic degradation percentages are 92.43%, 93.96%, 97.95% and 99.47%, respectively, and 20 mg is the optimized catalyst dose. As the irradiation time increased, the MB dye concentration declined (Fig. 5**b**). The results demonstrated that as the catalyst dosage was raised, the photocatalytic efficiency rose linearly. The degradation efficiency was enhanced when the catalyst load was raised from 5 to 20 mg. Fewer photons are absorbed by $CuMoO_4$ for the photocatalytic process when the catalyst amount is low, resulting in decreased photocatalytic activity. With higher catalyst loading, there are more photon absorption and activity centres on the $CuMoO_4$ surface, which in turn raises the catalyst's activity. However, the quantity of photons tends to become saturated as the loading of catalysts rises [30].

The kinetics of MB degradation were investigated further by comparing the photocatalytic activity of $CuMoO_4$ employing the Langmuir-Hinshelwood rate equation. As shown in Eq. 4, the MB degradation followed pseudo-first-order (PFO) kinetics [31].

$$-ln\ (C_o/C) = kt \tag{4}$$

where C_0 and C_t are the starting and final concentrations, at a particular irradiation period, respectively, and k is the PFO rate constant.

Fig. 5**c** displays the kinetic fits for the MB dye degradation using various catalyst doses of 0.3 M $CuMoO_4$ such as 5, 10, 15, and 20 mg. As a result of fitting *ln* (C_0/C) *vs.* irradiation time with a linear function, the values of k and R^2 were determined and listed in **Table S1.** The rate

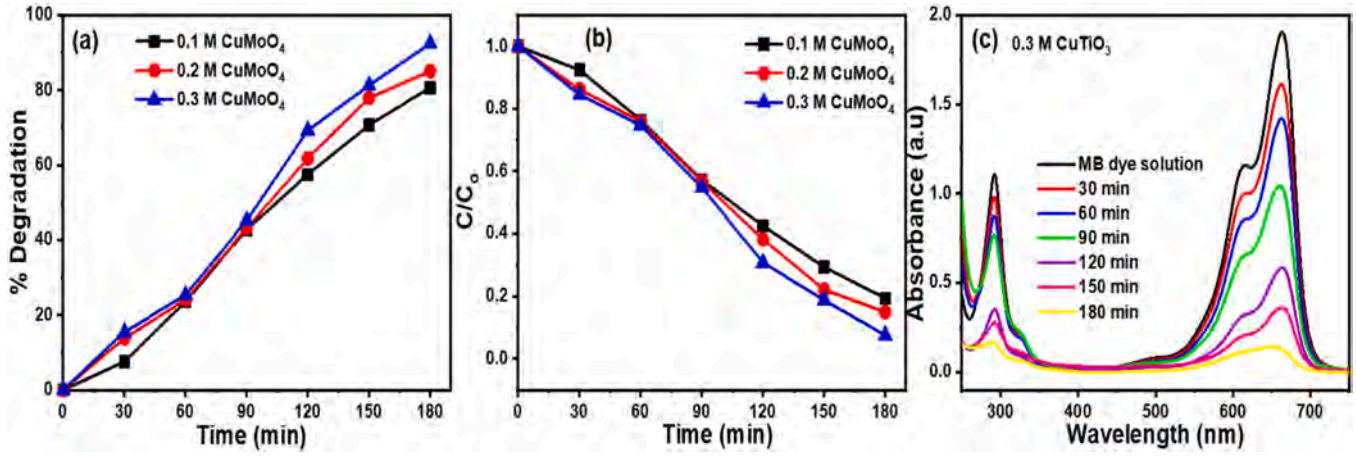

Fig. 4. (a) MB dye degrading efficiency of various catalysts at 30-minute time intervals up to 180 min, (b) plot of C/C_o *vs.* irradiation time for the photocatalytic degradation of MB dye using various catalysts, (c) UV–vis absorption spectra of 10 ppm MB dye degradation employing 5 mg of the 0.3 M $CuMoO_4$ NPs at natural pH.

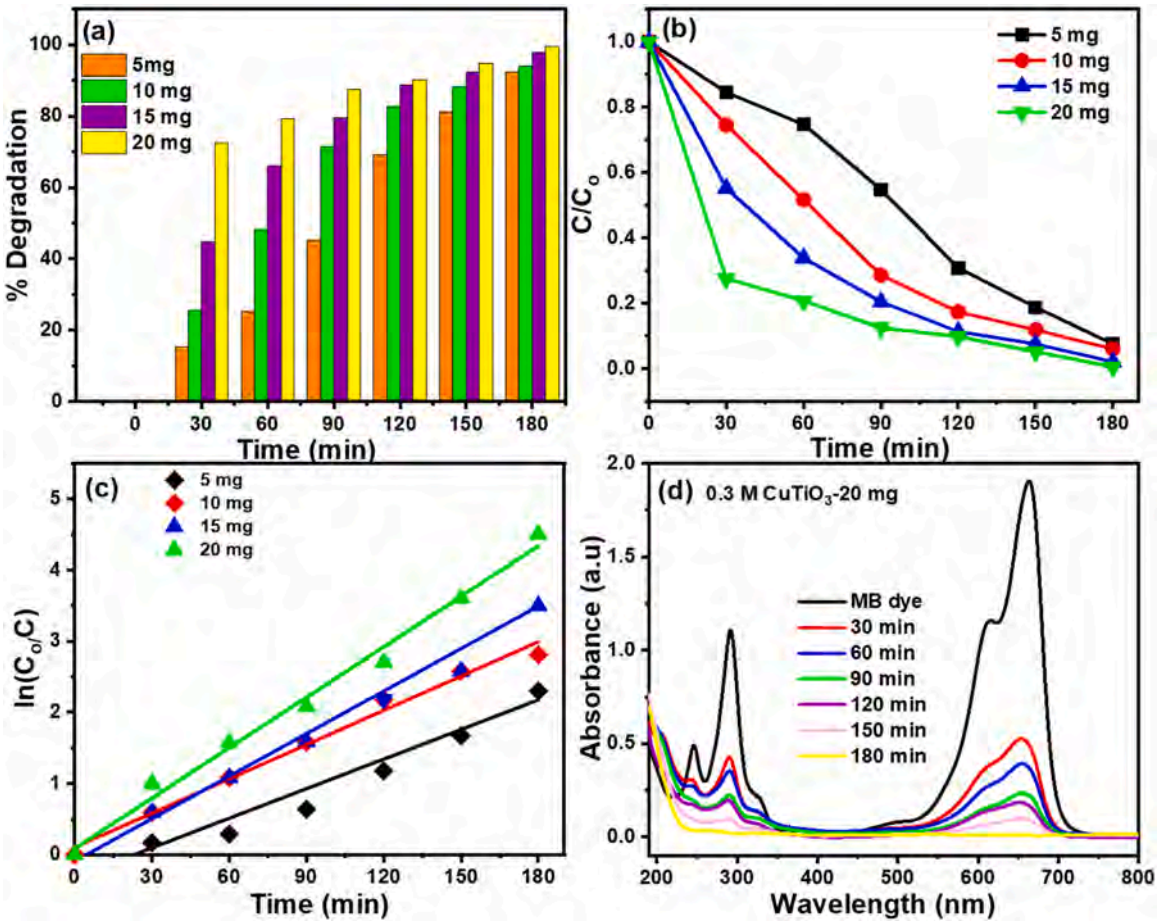

Fig. 5. (a) Degrading efficiency of various catalyst doses, (b) plot of C/C_o *vs.* irradiation time, (c) plots of *ln* (C_o/C) *vs.* reaction time for photocatalytic degradation of MB dye using various catalyst doses, (d) UV–vis absorption spectra of 10 ppm MB dye degradation using 20 mg of the 0.3 M $CuMoO_4$ NPs at natural pH.

constants for various catalyst doses of 0.3 M $CuMoO_4$ as well as the related correlation coefficients. In comparison to 5, 10, and 15 mg, the calculated rate constant value of 20 mg was determined to be higher, while among all catalyst doses, the 20 mg displayed the large value of k within 180 min of irradiation time. Fig. 5**d** displays the absorption spectra for the optimal 20 mg catalyst dosage of 0.3 M $CuMoO_4$ NPs for photocatalytic degradation MB dye. The results showed as the catalyst dose increases, the rate of MB degradation increases. The 0.3 M $CuMoO_4$ catalyst loading is 20 mg, which is the optimal catalyst dose with 10 ppm dye solution at natural experimental conditions for the following study.

3.7.2. *Effect of MB concentration*

The photocatalytic deterioration of organic dyes is dependent on the organic dye adsorption onto the photocatalyst surface, hence only the quantity of dye adsorbed onto the surface of the photocatalyst will take part. By studying the photocatalytic degradation at various organic dye concentrations, such as 10, 20, 30, and 40 ppm, it was possible to determine the influence of organic dye concentrations on the photocatalytic activity of 0.3 M $CuMoO_4$. The experiment is conducted using 20 mg (fixed) of 0.3 M $CuMoO_4$ catalyst to the different starting dye concentrations, such as 10, 20, 30, and 40 ppm while maintaining the dye solution at natural pH (Fig. 6**a-d**). Fig. 6**a** depicts degradation percentages of the MB dye solution at 10, 20, 30, and 40 ppm, with 99.47%, 93.76%, 88.06%, and 80.37%, respectively. The MB dye concentration decreased as the irradiation period increased (Fig. 6**b**). The maximum degradations were achieved at 10 ppm, as displayed in Fig. 6**c's** plot of the *ln* (C_0/C) *vs.* irradiation time for various starting dye degradation. **Table S2** shows values of k and R^2 for different MB dye concentrations using 20 mg of 0.3 M $CuMoO_4$ at natural pH. The absorption spectra for the optimum 10 ppm MB dye solution using a 20 mg catalyst dose of 0.3 M $CuMoO_4$ NPs at natural pH are shown in Fig. 6**d**. The rate of dye photodegradation is influenced by the possibility of $^{\bullet}OH$ radical generation on the surface of the $CuMoO_4$ and the reaction rate of MB molecules with the $^{\bullet}OH$ radical. Increases in dye concentration from 20–40 ppm reduce the catalyst's activity. This may be because more MB adsorbed on the surface of $CuMoO_4$ NPs at high dye concentrations, inhibiting the reaction among the dye molecules and $^{\bullet}OH$ radicals and decreasing the amount of $^{\bullet}OH$ radicals formed [32]. The findings revealed that the 10 ppm MB dye solution and 20 mg catalyst dosage at natural pH were fixed for further experiments.

3.7.3. *Effect of pH and pH_{ZPC}*

The solution pH is a crucial parameter for analyzing dye mineralization as it gives an idea about the surface charge on $CuMoO_4$. The MB mineralization at various pH levels of 3, 5, 7, 9, and 11 was examined while keeping the 20 mg 0.3 M $CuMoO_4$ catalyst dose and a 10 ppm MB solution. The MB mineralization at pH levels of 3, 5, 7, 9, and 11 is shown in Fig. 7**a**, with values of 97.42%, 97.95%, 99.47%, 98.84%, and 97.79%, respectively. Fig. 7**b** displays the C/C_o plot of the photodegradation activity of the $CuMoO_4$ sample against MB mineralization at pH-3, 5, 7, 9, and 11, as the irradiation time increased, the concentration of MB dye decreased. Fig. 7**c** displays the plot of the *ln* (C_0/C) *vs.* irradiation time, and kinetic fits for MB degradation using different pH of 10 ppm MB dye solution utilizing 20 mg of 0.3 M $CuMoO_4$ NPs. The rate constants and correlation coefficients (R^2) for various pH solutions of MB dye using 20 mg of 0.3 M $CuMoO_4$ are shown in **Table S3**. Fig. 7**d** displays absorption spectra for an optimal 10 ppm MB dye solution with

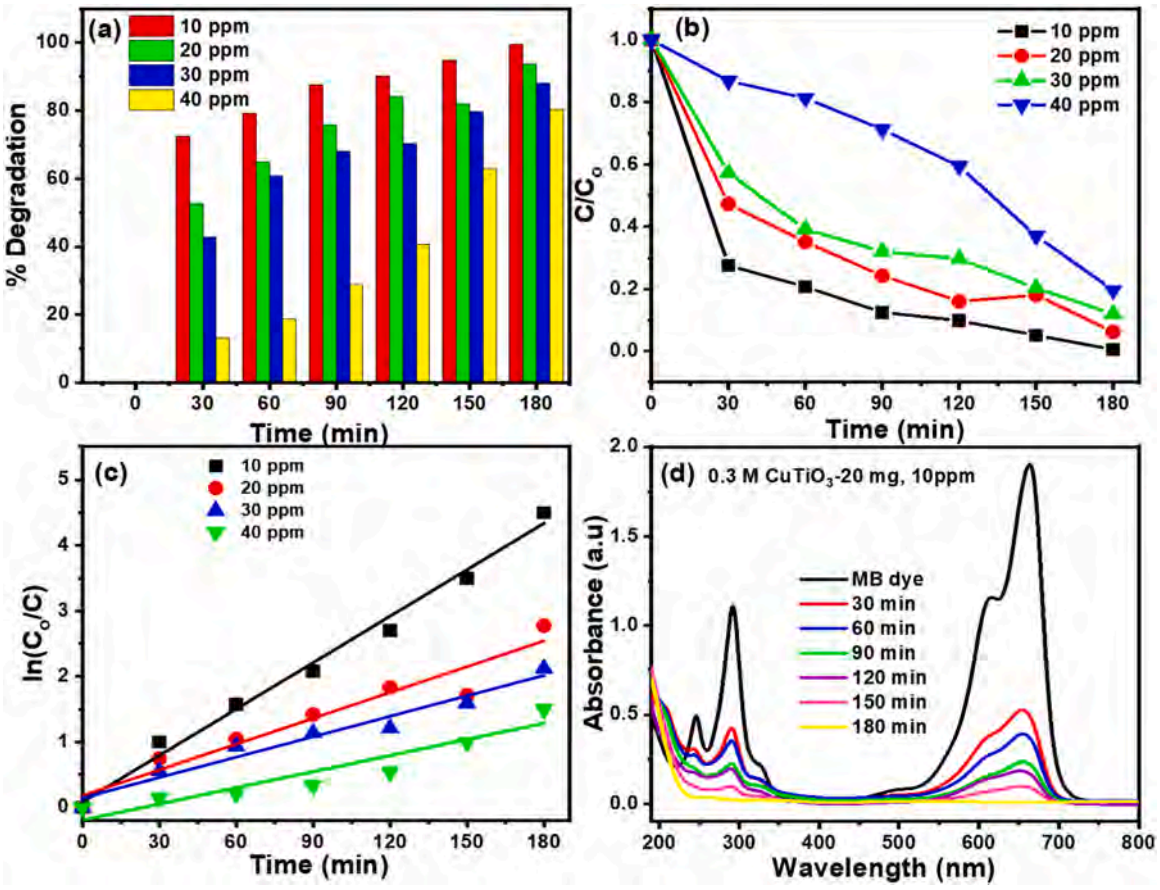

Fig. 6. (a) Degrading efficiency of various concentrations of MB dye, (b) plot of C/C_o *vs.* irradiation time, (c) plots of *ln* (C_o/C) *vs.* reaction time for photocatalytic degradation of MB dye using various concentrations of MB dye, (d) UV–vis absorption spectra of 10 ppm MB dye degradation using 20 mg of the 0.3 M $CuMoO_4$ NPs at natural pH.

a catalyst dosage of 20 mg of 0.3 M CuMoO4 NPs at pH 7. From pH 3 to pH 7, the degradation efficiency increases. The removal efficiency decreases at acidic pH owing to 0.3 M $CuMoO_4$ dissolution at pH 3. At pH 7.05, 0.3 M $CuMoO_4$ has a pH_{ZPC} (Fig. 8**a**). Above pH_{ZPC}, the surface of 0.3 M $CuMoO_4$ is more negatively charged, while MB has a positive charge in an aqueous solution. The highest efficiency for MB dye is seen at pH 7, which may be due to the dye molecules having significant interaction with the catalyst surface at this pH level. MB dye degrades most effectively at pH-7, degrading up to 99.47% of the dye after 180 min of irradiation [32]. Hence 10 ppm MB dye solution and 20 mg catalyst dosage at pH 7 were fixed for further study..

3.7.4. Scavenger study

It is widely known from the literature that when semiconductors are exposed to radiation, they produce $O_2^{\bullet-}$, $^{\bullet}OH$, e^-, and h^+. These species may then interact with organic contaminants to break them down into CO_2 and water. Trapping tests were performed to find out the species involved in the degradation of MB to prove the reaction mechanisms of the 0.3 M $CuMoO_4$ NPs in detail. In this regard, an aqueous suspension of MB was exposed to radiation in the presence of 0.3 M $CuMoO_4$ NPs containing various quenchers ($O_2^{\bullet-}$, h^+, e^-, and $^{\bullet}OH$), including benzoquinone (BQ), disodium ethylenediaminetetraacetate (EDTA-2Na), silver nitrate ($AgNO_3$), and isopropyl alcohol (IPA). The samples were obtained and spectrophotometrically monitored as usual. Fig. 8**b** depicts the percentage of MB degradation concerning the irradiation period in the absence and presence of various quenchers. The reaction rates for $AgNO_3$ (e^-), Na_2-EDTA (h^+), P-BQ ($^{\bullet}O_2^-$), and IPA ($^{\bullet}OH$) are 89.86%, 77.88%, 25.31%, and 45.22%, respectively. The reaction efficiency of the synthesized 0.3 M $CuMoO_4$ NPs was inhibited more by the addition of P-BQ and IPA to the photocatalytic process as an $^{\bullet}O_2^-$ and $^{\bullet}OH$ species hunter, indicating that photogenerated superoxide and hydroxyl radicals play an important role in the photodegradation process. $AgNO_3$ and EDTA had little effect on the degradation, proving that the electron and hole are not the primary reactive species responsible for the oxidation of the organic contaminants. In contrast, BQ and IPA can suppress the reaction, showing that $O_2^{\bullet-}$ and $^{\bullet}OH$ play a role in dye mineralization [31]. These radicals formation confirms indirect photocatalysis, similar results have been reported in the literature [39,40].

3.7.5. Mechanism of MB degradation

Based on the findings from the scavenger experiment and the band gap of 0.3 M $CuMoO_4$ NPs as shown in Scheme 2, (see the valence band and conduction band calculation in the S file) the proposed degradation mechanism for the separation of charges and photocatalytic reactions of MB dye employing 0.3 M $CuMoO_4$ NPs under sunlight irradiation can thus be proposed:

$$CuMoO_4 + h\nu \rightarrow e^- + h^+ \quad (5)$$

$$e^- + O_2 \rightarrow O_2^{\bullet-} \quad (6)$$

$$(H_2O \leftrightarrows H^+ + OH^-) + h^+ \rightarrow H^+ + {}^{\bullet}OH \quad (7)$$

$$MB + O_2^{\bullet-}/{}^{\bullet}OH/h^+ \rightarrow \text{intermediates} \rightarrow \text{degradation products} \quad (8)$$

In the first stage, photogenerated holes (h^+) and electrons (e^-) formed on the surface of $CuMoO_4$ particles (Eq. 5). Many published studies show that two oxidative agents $O_2^{\bullet-}$ and $^{\bullet}OH$ radicals are mostly concerned when exposed to sunlight. Photogenerated electrons and holes then interacted with water and DO to produce $O_2^{\bullet-}$ radicals as well

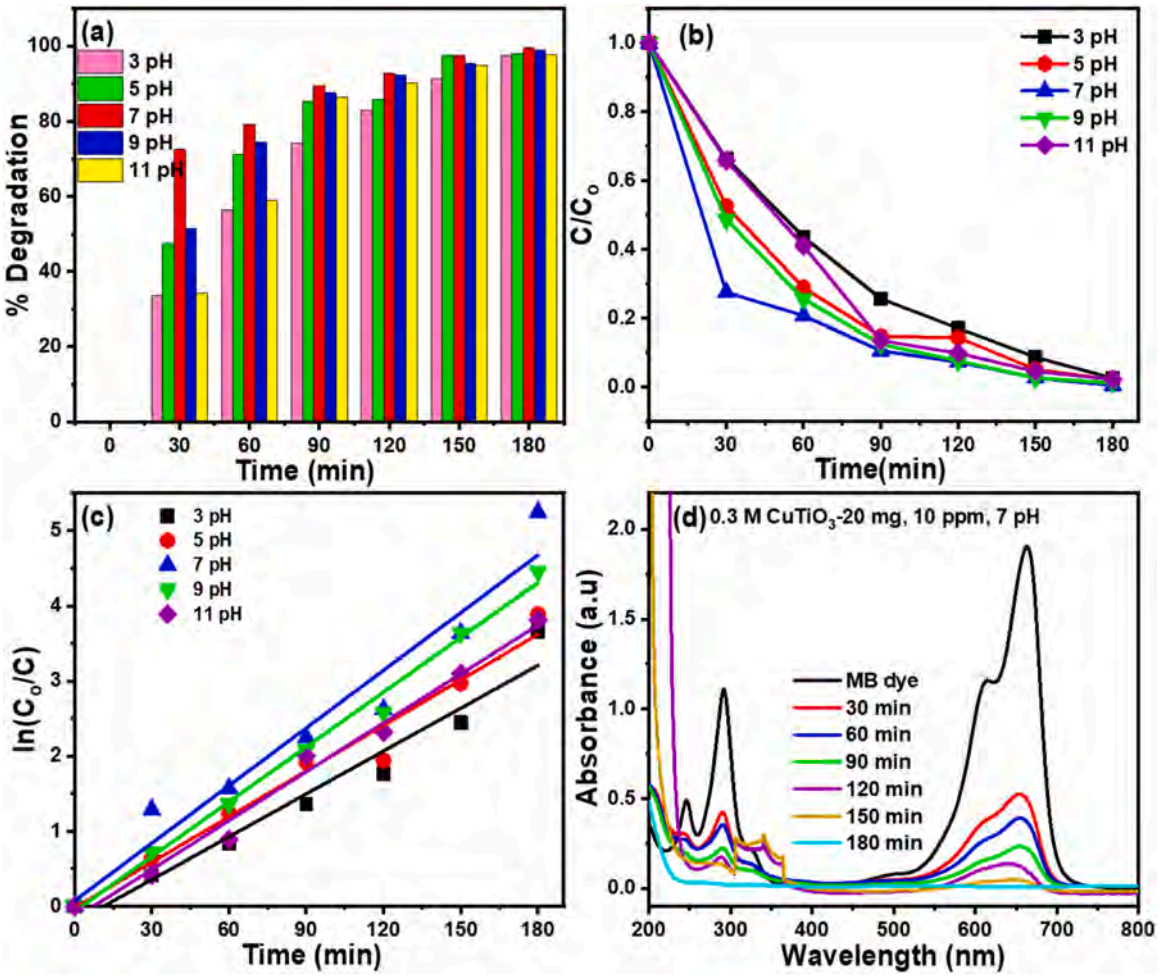

Fig. 7. (a) Degrading efficiency of various pH levels of MB dye, (b) plot of C/C_o *vs.* irradiation time, (c) plots of *ln* (C_o/C) *vs.* reaction time for photocatalytic degradation of MB dye using various pH levels, (d) UV–vis absorption spectra of 10 ppm MB dye degradation using 20 mg of the 0.3 M $CuMoO_4$ NPs at pH 7. Table 1 shows the results of a comparative study of our work.

as $^{\bullet}OH$ radicals (Eqs. 6 and 7). $O_2^{\bullet-}$ was the most active radical in the photocatalytic reaction. The solution's free radicals then interacted with MB forming intermediate compounds, which were then degraded into smaller molecules (Eq. 8) [14].

3.7.6. *Degradation pathway of MB dye*

The photocatalytic breakdown of MB in aqueous media under sunlight irradiation was studied. There are several intermediates that possibly led to the degradation of MB, from more complex to simpler ones and environmentally friendly in nature. LCMS has identified the following intermediate compounds, which are displayed in Fig. 9. The relevant compounds and their structural formulae were identified from the mass spectra based on the ratios of mass to charge (m/z). Scheme 3 proposes the photocatalytic degradation path of MB dye ($m/z = 320$). The following reactions may occur during the degradation process: (1) cleavage of the -N-double bond, (2) cleavage of the benzene ring, (3) cleavage of the C-N and C-C bonds of the chromophoric group, and (4) cleavage of the C-S link between the aromatic ring and the sulfonate groups [41].

3.7.7. *Stability*

A catalyst's stability can be greatly influenced by its capacity to be recycled. The stability of $CuMoO_4$ was assessed by utilizing the most active photocatalysts (0.3 M $CuMoO_4$) for four consecutive cycles for degradation of MB under the same conditions as in the photocatalytic experiment. Fig. 8**c** shows the photocatalyst's performance loss after four successive cycle runs, showing the catalyst's strong stability throughout the photocatalytic reaction when exposed to sunlight [42]. After the photocatalytic study, the physical and chemical stabilities of the photocatalyst were also examined. The nanocrystals' chemical structure (shown by the XRD patterns in Fig. 8**d**) has a similar, though small, crystallinity loss to that of freshly synthesized NPs. The catalyst's decreased crystallinity after the 4th photocatalytic dye degradation cycle might be due to structural damage, surface contamination, or catalyst degradation caused by extended exposure to the reactive environment. The MB of the 0.3 M $CuMoO_4$ photocatalyst used as evidence supports this. This exhibits the structural stability and durability of the prepared photocatalyst, which are vital to practical application.

3.8. *Antibacterial activity of 0.3 M $CuMoO_4$ against Streptococcus mutans and Salmonella typhi*

The zone of inhibitions was determined to assess the test sample's efficiency as an antibacterial agent against *Salmonella typhi* and *Streptococcus mutans*. The test samples were examined for antibacterial activity using 0.3 M $CuMoO_4$ NPs. 0.3 M $CuMoO_4$ NPs showed modest effectiveness with a 1.2 mm zone of inhibition against *Streptococcus mutans* and also exhibited modest activity with an inhibitory zone of 0.8 mm against *Salmonella typhi*. Both bacterial strains were inhibited by standard streptomycin with a 2.2 mm zone of inhibition. Based on the antimicrobial activity studies, 0.3 M $CuMoO_4$ NPs are a moderately effective antimicrobial agent against *Salmonella typhi* and *Streptococcus*

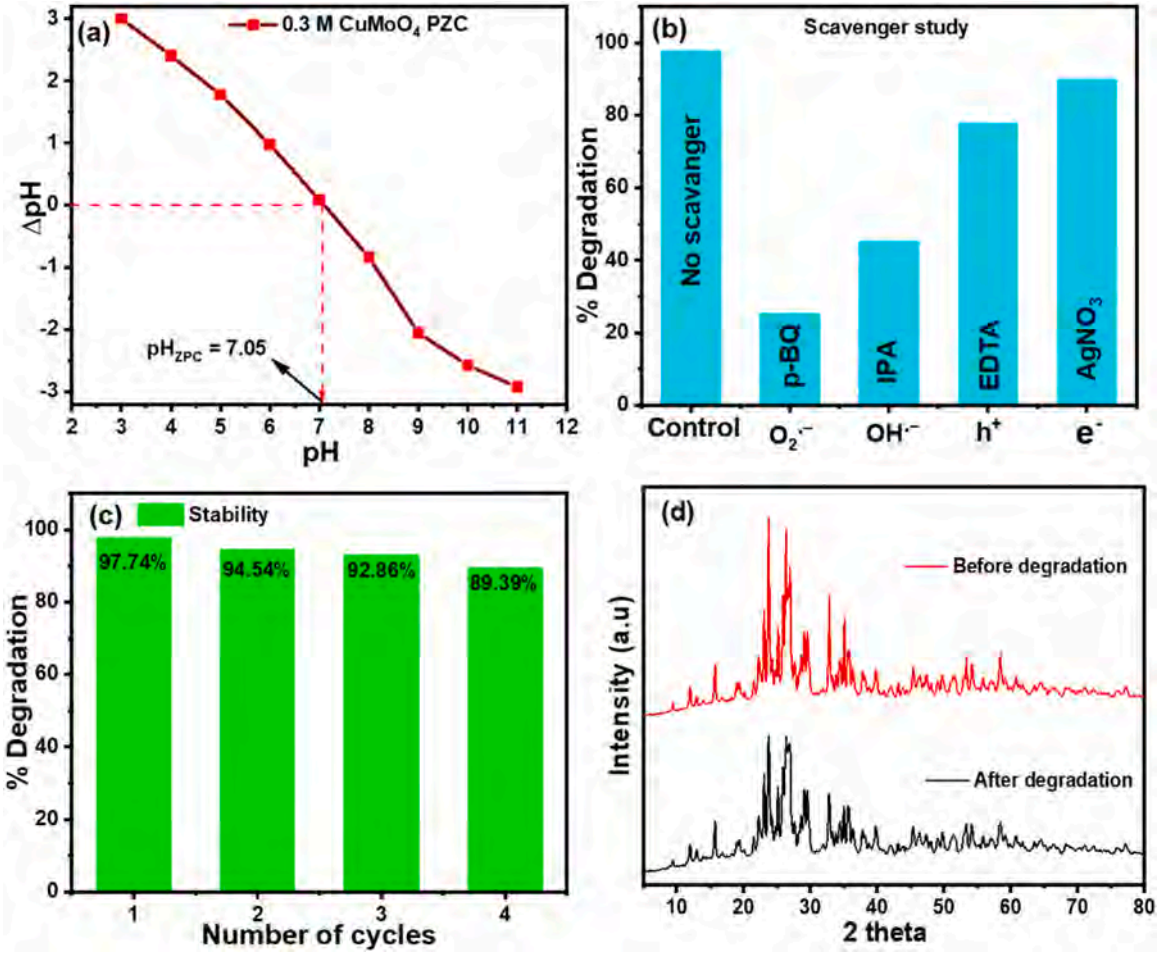

Fig. 8. (a) Point of Zero Charge (PZC) of 0.3 M $CuMoO_4$ NPs (b) effects of scavengers on the photocatalytic degradation performance of MB dye using 0.3 M $CuMoO_4$ NPs under sunlight irradiation. (c) Stability after four consecutive cycles, and (d) the XRD pattern, of fresh and recycled 0.3 M $CuMoO_4$ NPs.

Table 1
Comparison of photocatalytic performance of $CuMoO_4$ with reported literature.

Catalyst	Dye	Dose	(%) Degradation	Reaction Time (min)	Refs.
CuSnSe	MB	20 mg/ 20 mL	88.68	360	[33]
Sm-doped GO/ $KSrPO_4$	MB	1.5 mg/ mL	83.35	180	[34]
Na^+ co-doped $CaTiO_3:Eu^{3+}$	MB	2 mg/mL	96.62	300	[35]
NiO/Cr_2O_3	MB	50 mg/ 50 mL	93.63	180	[36]
Ag_2O/TiO_2	MB	50 mg/ 100 mL	95.4	180	[37]
$BaTiO_3$ @ZIF-8	MB	60 g/ 100 mL	93	180	[38]
$CuMoO_4$	MB	20 mg/ 100 mL	99.47	180	**This work**

mutans (Fig. 10). Table 2 shows the antibacterial activity results.

4. Conclusion

In summary, the novel synthetic process was used to synthesize $CuMoO_4$ with various concentrations of Cu. The band gaps of 0.1 $CuMoO_4$, 0.2 $CuMoO_4$, and 0.3 M $CuMoO_4$ were determined as 1.97 eV, 1.86 eV, and 1.44 eV, respectively. When compared to 0.1 $CuMoO_4$ and 0.2 M $CuMoO_4$, 0.3 M $CuMoO_4$ NPs showed red-shift to absorption edges and greater intensities in the visible light range. PL study showed that the recombination rate in 0.3 $CuMoO_4$ is lower than that of 0.1 $CuMoO_4$ and 0.2 M $CuMoO_4$ NPs. The XPS findings for $CuMoO_4$ showed that Cu, Mo, and O have chemical valence values of + 2, + 6, and 2, respectively. The degradation of MB with various Cu concentrations (0.1, 0.2 and 0.3 M) in $CuMoO_4$ as catalysts was studied. The 0.3 M $CuMoO_4$ is effectively employed as evidence suggesting to determine photocatalytic properties due to its strong conductivity, high electron transfer rate, and high electrochemical activity. 0.3 M $CuMoO_4$ displayed better photocatalytic activity than 0.1 $CuMoO_4$ and 0.2 M $CuMoO_4$, Because of the decreased rate of electron-hole recombination. UV–visible spectra revealed that photocatalytic degradation of MB dye was 99.47% in 180 min for 0.3 M $CuMoO_4$ NPs, respectively. An initial dye concentration of 10 mg/L, catalyst dosage of 20 mg/0.1 L, and natural pH of 7 are the optimal conditions for the photodegradation of the MB dye. The scavenger results suggested that $O_2^{\bullet}$ and $OH^{\bullet}$ played a key part in the photocatalytic degradation of MB dye and presented a photocatalytic degradation mechanism. The excellent extent of reusability of $CuMoO_4$ was shown by the cycling photocatalytic degradation of MB. 0.3 M $CuMoO_4$ was shown to be a moderately effective antibacterial agent against the gram-negative *Streptococcus mutans*, and gram-positive *Salmonella typhi*. Based on the findings, 0.3 M $CuMoO_4$ NPs have been found as a promising option that is stable, reusable, and, most importantly, can be employed for photocatalytic degradation of organic contaminants.

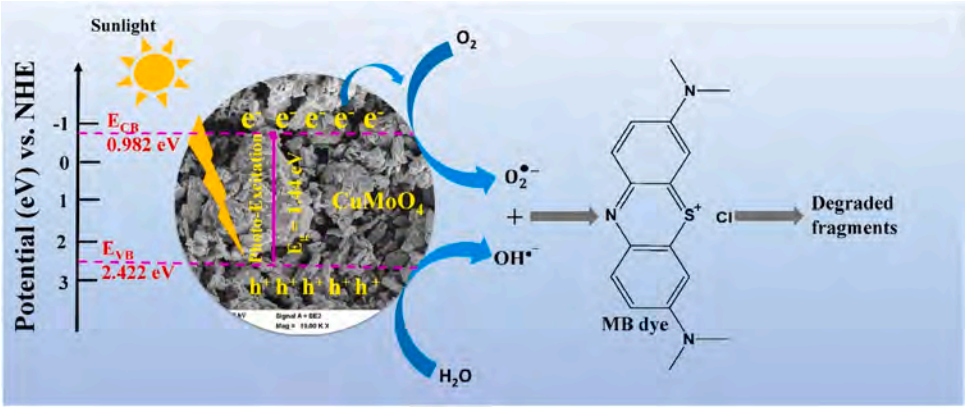

Scheme 2. Reaction mechanism of MB dye using $CuMoO_4$ NPs under sunlight irradiation.

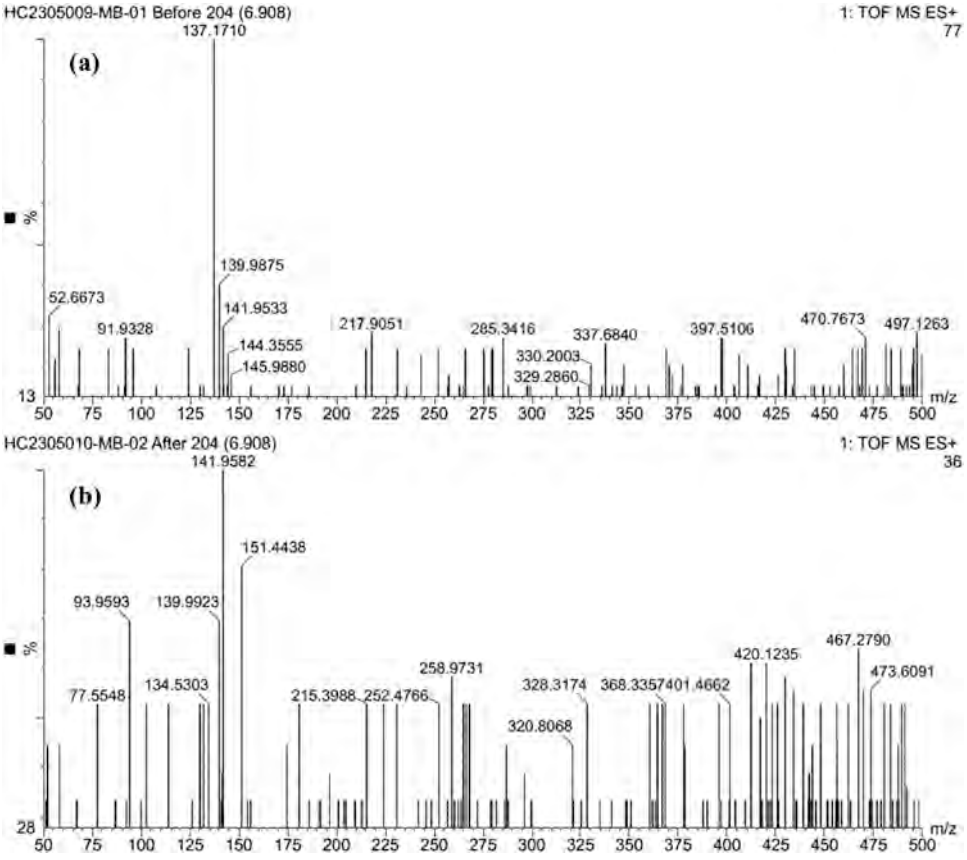

Fig. 9. Mass spectra of MB dye (a) before and (b) after degradation.

Ethical approval

Not applicable.

Consent to participate

Not applicable.

Consent for publication

Not applicable.

Funding

The authors gratefully acknowledge the financial support from the Researchers Supporting Project Number (RSP2023R442), King Saud University, Riyadh, Saudi Arabia.

CRediT authorship contribution statement

Rusul Alabada: Experiments and Writing – original draft. **Asif Ayub:** Writing – review & editing, Methodology. **Yathrib Ajaj:** LC-MS study and interpretation. **Subrahmanya Ishwar Bhat:** Helped in revision. **Riyadh H. Alshammari:** Funding acquisition. **Aigul Abduldayeva:** Software, Investigation. **Ali Imran Mallhi:** Formal analysis. **Zubair Ahmad:** Supervision. **Rasha M.K. Mohamed:**

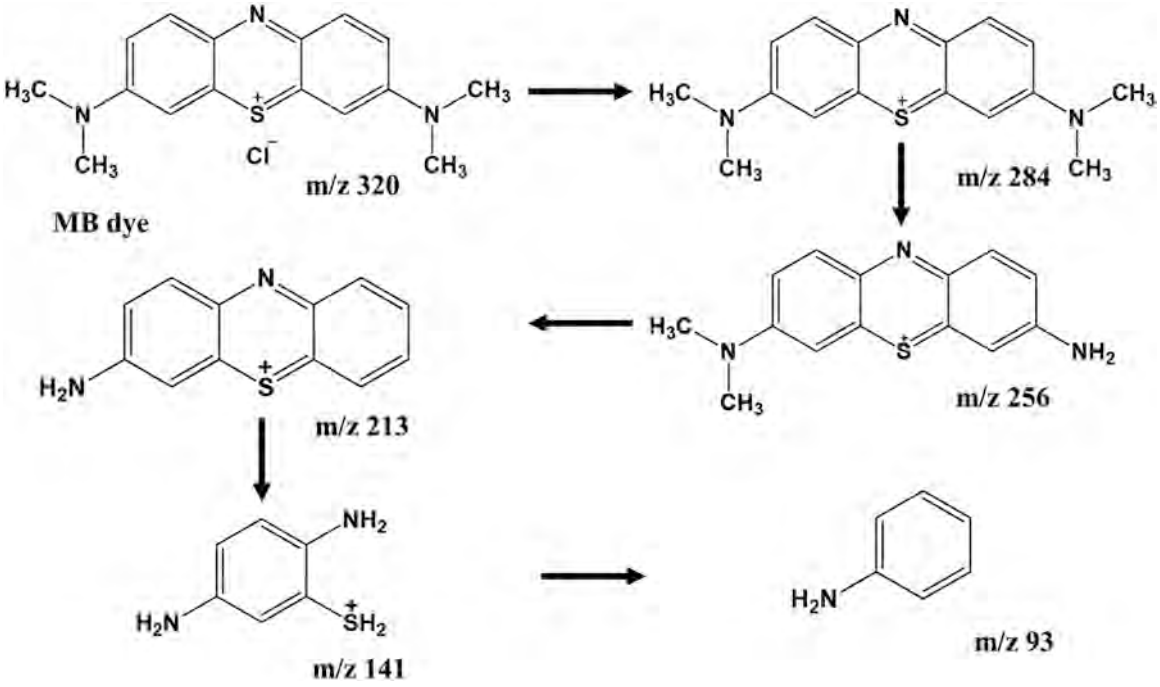

Scheme 3. Possible degradation pathway showing different intermediates of MB dye.

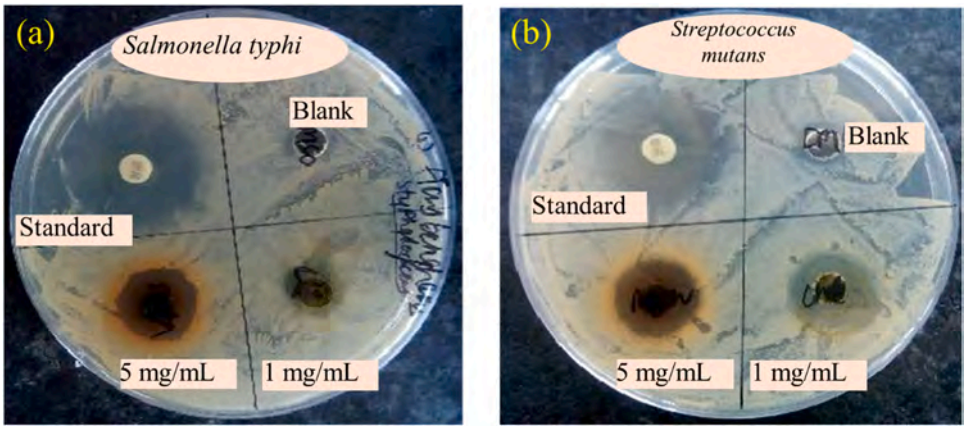

Fig. 10. Images of antibacterial results of 0.3 M $CuMoO_4$ NPs samples against *Salmonella typhi* and *Streptococcus mutans*.

Table 2
Percentage inhibition of samples against *Streptococcus mutans and Salmonella typhi*.

Sample	*Streptococcus mutans*			*Salmonella typhi*		
	Standard	Blank	5 mg/mL	Standard	Blank	5 mg/mL
0.3 M $CuMoO_4$	2.2	0	1.2	2.2	0	0.8

Conceptualization, Validation.

Declaration of Competing Interest

The authors declare that they have no known competing financial interests or personal relationships that could have appeared to influence the work reported in this paper.

Data availability

The datasets used and analyzed during the study are available from the corresponding author upon reasonable request.

References

[1] T.L. Nguyen, A. Ayub, A. Anam, A.M. Aljuwayid, S.W. Alwash, R. Abbass, A.A. K. Ruhaima, E. Potrich, M. Sillanpaa, S. Gul, R. Alshammari, S. Ullah, K. Ahmad, H. H. Pham Thi, Fabrication of ZnO decorated porous chitosan beads for the sustainable bioremediation of Cr(VI) contaminated water, J. Environ. Chem. Eng. 11 (2023) 110445, https://doi.org/10.1016/j.jece.2023.110445.
[2] H. Leelavathi, N. Abirami, R. Muralidharan, H.P. Kavitha, S. Tamizharasan, S. Sankeetha, R. Arulmozhi, Sunlight-assisted degradation of textile pollutants and phytotoxicity evaluation using mesoporous 11 (2021) 26800–26812, https://doi.org/10.1039/d1ra03806k.
[3] A.H. Jawad, R. Razuan, J.N. Appaturi, L.D. Wilson, Adsorption and mechanism study for methylene blue dye removal with carbonized watermelon (Citrullus lanatus)rind prepared via one-step liquid phase H_2SO_4 activation, Surf. Interfaces 16 (2019) 76–84, https://doi.org/10.1016/j.surfin.2019.04.012.
[4] A. Ayub, Z.A. Raza, Arsenic removal approaches: a focus on chitosan biosorption to conserve the water sources, Int. J. Biol. Macromol. 192 (2021) 1196–1216, https://doi.org/10.1016/j.ijbiomac.2021.10.050.

[5] A. Ayub, K. Srithilat, I. Fatima, N.M. Panduro-Tenazoa, I. Ahmed, M.U. Akhtar, W. Shabbir, K. Ahmad, A. Muhammad, Arsenic in drinking water: overview of removal strategies and role of chitosan biosorbent for its remediation, Environ. Sci. Pollut. Res. 29 (2022) 64312–64344, https://doi.org/10.1007/s11356-022-21988-z.

[6] A. Ayub, Z.A. Raza, M.I. Majeed, M.R. Tariq, A. Irfan, Development of sustainable magnetic chitosan biosorbent beads for kinetic remediation of arsenic contaminated water, Int. J. Biol. Macromol. 163 (2020) 603–617, https://doi.org/10.1016/j.ijbiomac.2020.06.287.

[7] F.M. Sanakousar, C. Vidyasagar, V.M. Jiménez-Pérez, K. Prakash, Recent progress on visible-light-driven metal and non-metal doped ZnO nanostructures for photocatalytic degradation of organic pollutants, Mater. Sci. Semicond. Process. 140 (2022) 106390, https://doi.org/10.1016/j.mssp.2021.106390.

[8] H.A. Kareem, M. Zaidi, A.A. Baqer, S.K. Hachim, T. ghazuan, K.K. Alasedi, N. M. Hameed, A.K.O. Aldulaim, M.K. Abid, M.J. Hussein, S.M.A. Dahesh, Synthesis and characterization of $CoFe_2O_4$ nanoparticles and its application in removal of reactive violet 5 from, Water, J. Nanostruct. 12 (2022) 521–528, https://doi.org/10.22052/JNS.2022.03.005.

[9] H.T. Mohammed, K. Kadhim Alasedi, R. Ruyid, S.A. Hussein, A.L. Jarallah, S.M. A. Dahesh, M.Q. Sultan, Z.N. Salman, B.S. Bashar, A. Kareem, O. Aldulaimi, M. A. Obaid, ZnO/Co_3O_4 nanocomposites: novel preparation, characterization, and their performance toward removal of antibiotics from wastewater, J. Nanostruct. 12 (2022) 503–509, https://doi.org/10.22052/JNS.2022.03.003.

[10] K. Bano, S.K. Mittal, P.P. Singh, S. Kaushal, Sunlight driven photocatalytic degradation of organic pollutants using a $MnV_2O_6/BiVO_4$ heterojunction: mechanistic perception and degradation pathways, Nanoscale Adv. 3 (2021) 6446–6458, https://doi.org/10.1039/d1na00499a.

[11] M. Dargahi, M. Masteri-Farahani, S. Shahsavarifar, M. Feizi, Microemulsion-mediated preparation of $Ce_2(MoO_4)_3$ nanoparticles for photocatalytic degradation of crystal violet in aqueous solution, Environ. Sci. Pollut. Res. 27 (2020) 12047–12054, https://doi.org/10.1007/s11356-020-07816-2.

[12] J.L.S. Junior, F.X. Nobre, F.A. De Freitas, T.A.F. De Carvalho, S.S. De Barros, C. Nascimento, L. Manzato, J.M.E. Matos, W.R. Brito, Y. Leyet, P.R.C. Couceiro, Ultrasonics Sonochemistry Copper molybdate synthesized by sonochemistry route at room temperature as an efficient solid catalyst for esterification of oleic acid, Ultrason. Sonochem. 73 (2021) 105541, https://doi.org/10.1016/j.ultsonch.2021.105541.

[13] H. Oudghiri, M. Akouibaa, S. Rakass, M. Abboudi, Journal of science: advanced materials and devices short communication a simple and cost-effective new synthesis method of copper molybdate $CuMoO_4$ nanoparticles and their catalytic performance, J. Sci. Adv. Mater. Devices 6 (2021) 501–507, https://doi.org/10.1016/j.jsamd.2021.06.003.

[14] W. Tan, J. Luan, Investigation into the synthesis conditions of $CuMoO_4$ by an: in situ method and its photocatalytic properties under visible light irradiation, RSC Adv. 10 (2020) 9745–9759, https://doi.org/10.1039/d0ra00496k.

[15] M.T. Islam, A. Dominguez, B. Alvarado-Tenorio, R.A. Bernal, M.O. Montes, J. C. Noveron, Sucrose-mediated fast synthesis of zinc oxide nanoparticles for the photocatalytic degradation of organic pollutants in water, ACS Omega 4 (2019) 6560–6572, https://doi.org/10.1021/acsomega.9b00023.

[16] W. Xu, A. Li, Y. Liu, R. Chen, W. Li, $CuMoO_4$@hexagonal boron nitride hybrid: an ecofriendly flame retardant for polyurethane elastomer, J. Mater. Sci. 53 (2018) 11265–11279, https://doi.org/10.1007/s10853-018-2390-5.

[17] S.P. Keerthana, B.J. Rani, R. Yuvakkumar, G. Ravi, Y. Shivatharsiny, E.S. Babu, H. S. Almoallim, S. Ali, D. Velauthapillai, ScienceDirect Copper molybdate nanoparticles for electrochemical water splitting application, Int. J. Hydrog. Energy 46 (2020) 7701–7711, https://doi.org/10.1016/j.ijhydene.2020.12.029.

[18] R. Sagheer, M. Khalil, V. Abbas, Z.N. Kayani, U. Tariq, F. Ashraf, Effect of Mg doping on structural, morphological, optical and thermal properties of ZnO nanoparticles, Opt. (Stuttg.) 200 (2020) 163428, https://doi.org/10.1016/j.ijleo.2019.163428.

[19] Z. Xia, J. Min, S. Zhou, H. Ma, B. Zhang, X. Tang, Photocatalytic performance and antibacterial mechanism of Cu / Ag-molybdate powder material, Ceram. Int. 47 (2021) 12667–12679, https://doi.org/10.1016/j.ceramint.2021.01.127.

[20] M. Ismail, S. Gul, M.I. Khan, M.A. Khan, A.M. Asiri, S.B. Khan, Green synthesis of zerovalent copper nanoparticles for efficient reduction of toxic azo dyes congo red and methyl orange, Green. Process. Synth. 8 (2019) 135–143, https://doi.org/10.1515/gps-2018-0038.

[21] U. Alam, A. Khan, D. Ali, D. Bahnemann, M. Muneer, Comparative photocatalytic activity of sol-gel derived rare earth metal (La, Nd, Sm and Dy)-doped ZnO photocatalysts for degradation of dyes, RSC Adv. 8 (2018) 17582–17594, https://doi.org/10.1039/c8ra01638k.

[22] N. Manjula, M. Pugalenthi, V.S. Nagarethinam, K. Usharani, A.R. Balu, Effect of doping concentration on the structural, morphological, optical and electrical properties of Mn-doped CdO thin films, Mater. Sci. Pol. 33 (2015) 774–781, https://doi.org/10.1515/msp-2015-0115.

[23] F.M. Sanakousar, C.C. Vidyasagar, S. Shikandar, V.M. Jiménez-Pérez, Mounesh, C. C. Viswanath, K. Prakash, Thermal decomposition synthesis of cylindrical rod-like $MoO_3$and irregular sphere-like Ag_2MoO_4nanocrystals for accelerating photocatalytic degradation of industrial reactive dyes and biosensing application, J. Environ. Chem. Eng. 11 (2023), https://doi.org/10.1016/j.jece.2023.109371.

[24] M.F. Sanakousar, C.C. Vidyasagar, V.M. Jiménez-Pérez, N. Mounesh, A. H. Shridhar, Mechanistic insight into the photocatalytic degradation of organic pollutants and electrochemical behavior of modified MWCNTs/Cu-Co_3O_4 nanocomposites, React. Chem. Eng. 7 (2022) 1847–1872, https://doi.org/10.1039/d2re00117a.

[25] Z. Shahri, M. Salavati-Niasari, N. Mir, G. Kianpour, Facile synthesis and characterization of nanostructured flower-like copper molybdate by the co-precipitation method, J. Cryst. Growth 386 (2014) 80–87, https://doi.org/10.1016/j.jcrysgro.2013.09.031.

[26] A. Modwi, L. Khezami, K.K. Taha, A.J. Bessadok, S. Mokraoui, Photo-degradation of a mixture of dyes using Barium doped ZnO nanoparticles, J. Mater. Sci. Mater. Electron. 30 (2019) 14714–14725, https://doi.org/10.1007/s10854-019-01843-7.

[27] F.M. Sanakousar, C.C. Vidyasagar, S.C. Swapna, V.M. Jiménez-Pérez, C. C. Viswanath, K. Prakash, M.B. Sridhara, Effect of surfactant on structural and optical properties of V_2O_5 nanocrystals as a potential catalyst for photodegradation, Iran. J. Catal. 13 (2023) 57–72, https://doi.org/10.30495/ijc.2023.1973011.1975.

[28] J. Cheng, L. Han, Y. Wei, Q. Chen, Enhancement of photocatalytic property on ZnS / MoS_2 composite under visible light irradiation, MATEC Web Conf. 108 (2017) 01008, https://doi.org/10.1051/matecconf/201710801008.

[29] S.F. Tadesse, D.H. Kuo, W.L. Kebede, L.W. Duresa, Synthesis and characterization of vanadium-doped $Mo(O,S)_2$ oxysulfide for efficient photocatalytic degradation of organic dyes, N. J. Chem. 44 (2020) 19868–19879, https://doi.org/10.1039/d0nj02565h.

[30] D. Zhang, S. Lv, Z. Luo, A study on the photocatalytic degradation performance of a $[KNbO_3]_{0.9}$-$[BaNi_{0.5}Nb_{0.5}O_{3-\delta}]_{0.1}$ perovskite, RSC Adv. 10 (2020) 1275–1280, https://doi.org/10.1039/c9ra07310h.

[31] A. Khan, M. Danish, U. Alam, S. Zafar, M. Muneer, Facile synthesis of a Z-Scheme $ZnIn_2S_4/MoO_3$ heterojunction with enhanced photocatalytic activity under visible light irradiation, ACS Omega 5 (2020) 8188–8199, https://doi.org/10.1021/acsomega.0c00446.

[32] L. Anju Chanu, W. Joychandra Singh, K. Jugeshwar Singh, K. Nomita Devi, Effect of operational parameters on the photocatalytic degradation of Methylene blue dye solution using manganese doped ZnO nanoparticles, Results Phys. 12 (2019) 1230–1237, https://doi.org/10.1016/j.rinp.2018.12.089.

[33] K. Patel, T. Parangi, G.K. Solanki, M.K. Mishra, K.D. Patel, V.M. Pathak, Photocatalytic degradation of methylene blue and crystal violet dyes under UV light irradiation by sonochemically synthesized CuSnSe nanocrystals, Eur. Phys. J. 136 (2021) 743, https://doi.org/10.1140/EPJP/S13360-021-01725-0.

[34] O. Oloye, J.F.S. Fernando, D. Golberg, A.P. O'Mullane, Sonochemical synthesis of Ga/ZnO nanomaterials from a liquid metal for photocatalytic applications, Adv. Sustain. Syst. 6 (2022) 2100312, https://doi.org/10.1002/ADSU.202100312.

[35] M. Chen, Q. Xiong, Z. Liu, K. Qiu, X. Xiao, Synthesis and photocatalytic activity of Na+ co-doped $CaTiO_3:Eu^{3+}$ photocatalysts for methylene blue degradation, Ceram. Int. 46 (2020) 12111–12119, https://doi.org/10.1016/J.CERAMINT.2020.01.256.

[36] S. Yadav, N. Rani, K. Saini, Synthesis and characterization of NiO/Cr_2O_3 nanocomposite with effective sunlight driven photocatalytic degradation of organic dyes, Environ. Sci. Pollut. Res. 30 (2023) 71957–71969, https://doi.org/10.1007/S11356-022-22746-X/FIGURES/8.

[37] S. Kavitha, R. Ranjith, N. Jayamani, Facile construction of novel Ag_2O combined TiO_2 nanocomposites with enhanced dye degradation under visible-light photocatalytic activity, Mater. Technol. 37 (2022) 1205–1219, https://doi.org/10.1080/10667857.2021.1928436.

[38] J. Swain, A. Priyadarshini, S. Hajra, S. Panda, J. Panda, R. Samantaray, Y. Yamauchi, M. Han, H.J. Kim, R. Sahu, Photocatalytic dye degradation by BaTiO3/zeolitic imidazolate framework composite, J. Alloy. Compd. 965 (2023) 171438, https://doi.org/10.1016/J.JALLCOM.2023.171438.

[39] A. Nisar, M. Saeed, M. Usman, M. Muneer, M. Adeel, I. Khan, J. Akhtar, Kinetic modeling of ZnO-rGO catalyzed degradation of methylene blue, Int. J. Chem. Kinet. 52 (2020) 645–654, https://doi.org/10.1002/kin.21389.

[40] M. Saeed, M. Muneer, N. Akram, A. ul Haq, N. Afzal, M. Hamayun, Synthesis and characterization of silver loaded alumina and evaluation of its photo catalytic activity on photo degradation of methylene blue dye, Chem. Eng. Res. Des. 148 (2019) 218–226, https://doi.org/10.1016/j.cherd.2019.06.020.

[41] A.S. Ganie, N. Bashar, S. Bano, S. Hijazi, S. Sultana, S. Sabir, M.Z. Khan, Development and application of redox active GO supported CeO_2/In_2O_3 nanocomposite for photocatalytic degradation of toxic dyes and electrochemical detection of sulfamaxole, Surf. Interfaces 38 (2023) 102774, https://doi.org/10.1016/j.surfin.2023.102774.

[42] M.F. Sanakousar, V. C.C, V.M. Jiménez-Pérez, B.K. Jayanna, Mounesh, A. H. Shridhar, K. Prakash, Efficient photocatalytic degradation of crystal violet dye and electrochemical performance of modified MWCNTs/Cd-ZnO nanoparticles with quantum chemical calculations, J. Hazard. Mater. Adv. 2 (2021) 100004, https://doi.org/10.1016/j.hazadv.2021.100004.